MedCrave
Step into the World of Research
Aeronautics and Aerospace Open Access Journal

Research Article

Open Access
CrossMark

An optical-scan method for measuring the as-installed surface port incidence angles for flush air data sensing (FADS) systems

Abstract

The Flush Air Data Sensing (FADS) System, where air data are inferred from non-intrusive surface pressure measurements, uses natural contours of the vehicle forebody, wing leading edge, or probe. Although multiple methods have been developed to derive airdata from the sensed pressure matrix, all methods rely on accurate knowledge of local surface contours at the port locations. One of the most well-developed solution methods curve-fits the surface pressure distribution against the associated surface incidence angles using a quasi-Newtonian model. The well-known "Triples" algorithm extracts airdata from the curve-fit model. This solution method requires precise knowledge of as-installed incidence angles, i.e. the angles between the surface normal and the longitudinal axis of the vehicle. This study investigates the feasibility and accuracy of using an inexpensive optical-scanning system to measure the in-situ FADS pressure ports surface incidence angles. Here, two legacy 3-D printed probe shapes, as previously tested during a series of very low-speed wind tunnel tests, were used to develop and evaluate this method. The shapes 1) a hemispherical head cylindrical forebody, and 2) a Rankine-Body, were scanned along the longitudinal axis and the resulting point-cloud was edited using open-source software to generate three concentric "loops" surrounding each surface port. Each annular loop was assumed as co-planar with the surface port, and the singular-value decomposition (SVD) was used calculate the local surface gradient vector from the null-space solution. From the resulting gradient vector, geometric relationships calculate the port's polar coordinates including the surface incidence angle. For both body contours the resulting calculations are compared to the "known" design surface angles as prescribed for the 3-D prints. Error plots are presented for each individual ring-set, and for the collected set using all three ring together. For the collected data sets, the incidence angle calculations are accurate to within a quarter-degree.

Keywords: FADS, airdata, Rankine-body, hemispherical head, incidence angle, optical-scan, singular value decomposition

Volume 8 Issue 1 - 2024

Stephen A Whitmore
Mechanical and Aerospace Engineering Department, Utah State University, USA

Correspondence: Stephen A Whitmore, Professor-Emeritus, Mechanical and Aerospace Engineering Department, Director, Propulsion Research Laboratory, Utah State University, USA, Tel +143579729, Email Stephen.whitmor@usu.edu

Received: February 23, 2024 | **Published:** March 06, 2024

Nomenclature

A = quasi-Newtonian model slope fit coefficient

$\tilde{A}$ =Point-cloud ring planar coefficient vector

B = quasi-Newtonian model bias fit coefficient

a, b, c = planar equation coordinate slopes

d = planar equation bias coefficient

$C_{P\theta}$ = coefficient of pressure, and incidence angle θ

$C_{P\max}$ = stagnation pressure coefficient

$\vec{i},\vec{j},\vec{k}$ = unit vectors in x, y, z directions

M = Matrix of scan point cloud data points

m = number points in point-cloud ring

Null(M) = Null Space of Matrix M

$\vec{N}$ = Surface gradient vector

$\vec{n}$ = unit vector on body surface (def. 1)

$\vec{n}$ = normalized gradient vector (def. 2)

n_x, n_y, n_z = normalized surface gradient components

S = Singular value matrix

SVD = singular value decomposition

R = polar radius coordinate, cm

Rc = gradient vector radius of curvature, cm

U = SVD left-singular matrix

V = SVD right-singular matrix

$\vec{V}$ = airspeed/velocity vector, m/s

x = Cartesian axial coordinate, cm

y = Cartesian lateral coordinate, cm

z = Cartesian vertical coordinate, cm

x_p = FADS Port axial coordinate, cm

y_p = FADS Port lateral coordinate, cm

z_p = FADS Port vertical coordinate, cm

x_{Rc} = Gradient vector origin axial coordinate, cm

y_{Rc} = Gradient vector origin lateral coordinate, cm

z_{Rc} = Gradient vector origin vertical coordinate, cm

α = angle-of-attack, deg

β = angle-of-sideslip, deg

ϕ = clock angle, deg

ϕ_P = FADS surface port clock angle, deg.

Θ = cone angle, deg.

Θ_P = FADS surface port cone angle, deg.

θ = surface incidence angle, deg

Introduction

Airmass reference data for flight vehicles traditionally referred to as airdata are critical measurement parameters for modern flight-vehicles. Historically, airdata measurements were performed using intrusive booms which extend beyond the local flow field of the aircraft and measure airmass velocities by direct stagnation of the flow via a pitot tube at the end of the boom. Flow incidence angles were measured using mechanical vanes attached to the probe. Localized aircraft-induced effects were removed through empirical calibration. While the booms performed well at making steady measurements at moderate airspeeds, their use becomes infeasible at high-mach numbers such as for reentry vehicle like the Space Shuttle and the SNC Dreamchaser. Similarly, for very low-seed vehicles like Unmanned Aerial Systems (UAS), with the associated small size and low wing loading traditional probes have the potential to significantly change UAS flight dynamics, including an increase in parasitic drag, and a significant change in the weight-and-balance. Also, at the low-airspeeds and dynamic pressures associated with UAS flight, probes and booms are susceptable to vibration, can be easily damaged by rough vehicle landings, may have alignment issues due to the flexible structures, and require multiple moving parts, with the associated response dynamics. Finally, for specialized vehicle requiring "stealthy" contours, like B-2 Bomber, the use of conventional intrusive probe-based airdata systems would compromise the low-observable vehicle radar signature. Thus for each of the above listed reasons, the development of an alternate, less intrusive, approach to airdata measurements is highly desirable.

Background

As a means of circumventing these and other difficulties with intrusive systems, the flush airdata sensing (FADS) system concept where airdata are inferred from nonintrusive surface pressure measurements. The use of a FADS system does not require probing of the local flow-field to compute air data parameters. Instead FADS uses the natural contours of the vehicle forebody or wing leading edge. This minimally-intrusive approach is ideal for UAS applications. Also, because the FADS system requires no moving parts, issues associated with dynamical response of the flow direction vanes and their associated potentiometer sensors do not exist. The original Shuttle Entry Airdata Systems (SEADS) was developed at the NASA Langley Research Center (NASA-Langley) for the space shuttle program.[1 3] This concept was later extended to a generic FADS configuration that was adapted to a wide swath of flight configurations.[4 7] Cobleigh et al.,[8] demonstrated that this approach can be applied to a wide variety of blunt-body shapes. The FADS system using the variational solution algorithms was applied to three premier hypersonic flight programs in the late 1990's, the X-33,[9] X38,[10] and X-43.[11] In 2017 a FADS system was developed and flight tested for the Sierra Nevada Corporation's Dream Chaser Space plane.[12]

For these early programs, the sensed pressures were related to the desired airdata parameters using a non-physical mapping. These tests verified the feasibility of the fixed orifice concept but did not demonstrate real time capable algorithms for estimating the airdata from the pressure measurements. The first estimation algorithms capable of real-time operation were developed at the NASA Dryden flight research center during the late 1980's and early 1990's for the F/A-18 High Alpha Research Vehicle (HARV) and System Research Aircraft SRA) programs. The estimation algorithms developed for the HARV program were first demonstrated in a real-time flight environment by Whitmore et al.,[13] The real-time solution algorithms for these early FADS systems fit the surface pressure distribution to a calibrated quasi-Newtonian model. The form of this simple model is convenient for calculating the airdata state from a measured surface pressure distribution using the well-known "Triples" algorithm.[9,13] This approach allows a closed-form inverse solution to be calculated in near real time, where the flow-direction angles were analytically solved for the flow incidence angles using groupings of three surface pressure ports. The remaining airdata vector was calculated using iterative least-squares.

Since those early programs a variety of alternative solution methods have been developed. Crowther and Lamont,[14] at the University of Manchester published a paper detailing their work on calibrating Neural Networks to interpret pressure data for an arbitrary fuselage design. At roughly the same time, Rohloff et al., published similar work using neural networks to calibrate flush airdata systems for blunt-nosed configurations.[15,16] Recently, Laurence and Argrow[17] successfully adapted a FADS systems of a Small UAS, the X-8 Skywalker. Computational fluid dynamics simulations were used to determine the port locations of the FADS. Airframe locations were sorted based on the total sensitivity over a range of angles of attack and sideslip. Multilayer feed forward neural networks were employed to produce estimates of the angle of attack and sideslip, while static and stagnation ports on the fuselage measured airspeed. Accurate results were reported for airspeeds as low as 25 m/sec.

FADS surface port layout considerations

Each of the above solution methods rely on accurate knowledge of the "as-installed" local surface contours at the port locations; specifically, the surface incidence angles, between the surface normal and the longitudinal axis of the vehicle. Figure 1 shows a typical generic 9-port FADS surface pressure port layout. For the quasi-Newtonian model,[18] the local surface pressure coefficient is related to the surface incidence angle by

$$Cp_\theta = Cp_{\max}\left(A.\cos^2\theta + B\right) \quad (1)$$

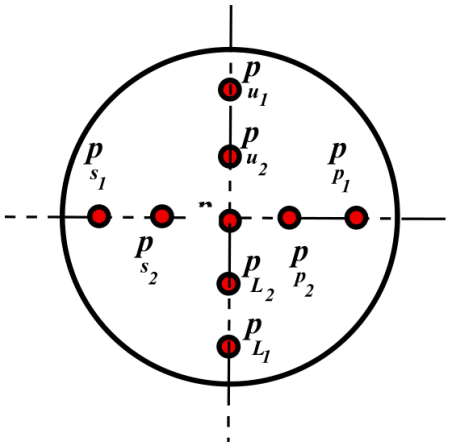

Figure 1 Generic 9-Port FADS pressure matrix layout.

where $Cp_{\max}$ is the compressible-flow stagnation pressure coefficient,[18] and the curve-fit parameters {A, B} are constrained to give A + B =1. The surface position of a particular pressure port can be described in terms of two polar coordinates, "cone" Θ and "clock" ϕ

angles. The total surface incidence angle θ at non-zero angle-of-attack α and/or sideslip β can be calculated by taking the inner product of the local flow direction vector and the surface normal,

$$\vec{V}.\vec{n} = \cos\theta = \begin{bmatrix} \cos\alpha\cos\beta\cos\Theta + \\ \sin\beta\sin\Theta\sin\phi + \\ \sin\alpha\cos\beta\sin\Theta\cos\phi \end{bmatrix} \quad (2)$$

$$\text{Where, } \vec{V} = \begin{bmatrix} u \\ v \\ w \end{bmatrix} = V_\infty \begin{bmatrix} \cos\alpha\cos\beta \\ \sin\beta \\ \sin\alpha\cos\beta \end{bmatrix} \vec{n} = \begin{bmatrix} \cos\Theta \\ \sin\Theta\sin\phi \\ \sin\Theta\cos\phi \end{bmatrix} \quad (3)$$

At zero angles-of-attack and -sideslip, $\theta = \Theta$. In order to calculate a complete airdata set including the flow direction angles, airspeed, and dynamic pressure, a matrix of at least 5 pressure ports is required. As described by[19,20] allowing for more ports gives a measure of noise rejection in the system, and allows for system redundancy in the case that a pressure sensor malfunctions.

Figure 2 shows the geometric definitions of the surface cone- and clock-angles. Here the $\{x_p, y_p, z_p\}$ is the surface port location as described by the vehicle coordinate system. R_c is the local radius-of-curvature of the surface at the port location, and $\{xR_c, yR_c, zRc\}$ is the origin point of the radius-of-curvature, ending at the point $\{x_p, y_p, z_p\}$. Assuming lateral symmetry, intercept of the radius-of-curvature with the vehicle longitudinal axis is $\{x_{Rc}, 0, 0\}$. The coordinate R is the physical distance from the port surface location to the vehicle longitudinal centerline at the point. Rc is the radius-of-curvature of the surface at the point $\{x_{Rc}, 0, 0\}$. Based on the depicted geometry the cone-angle, clock-angle, and radius-of-curvature can be written in terms of the Cartesian coordinates as

$$\tan\Theta_p = \frac{\left(y_p - y_{R_c}\right)}{\sin\phi_p\left(x_p - x_{R_c}\right)}$$

$$\tan\phi_p = \frac{y_p - y_{R_c}}{z_p - z_{R_c}} \quad (4)$$

$$R_c = \sqrt{(x_p - x_{R_c})^2 + (y_p - y_{R_c})^2 + (z_p - z_{R_c})^2}$$

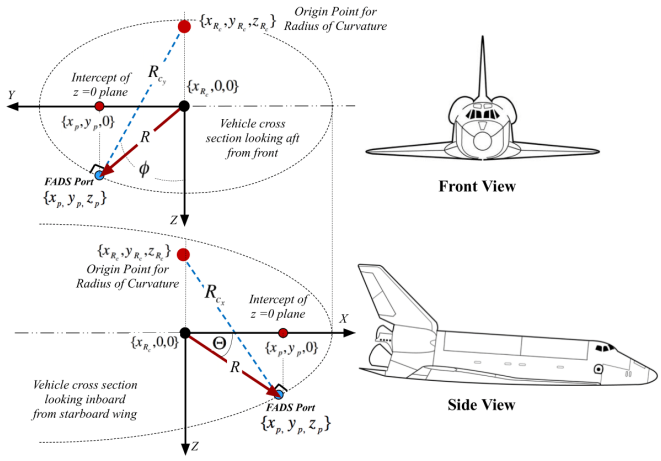

Figure 2 Cone- and clock-angle geometric definitions.

(Parts of this image taken from https://academic-accelerator.com/encyclopedia/space-shuttle-orbiter, reprinted with permission.)

For simple spherical nose cap configurations, such as was the case for the original Space Shuttle SEADS, determining the surface incidence angle was rather simple. However, for significantly more complex shapes, as is the case for the SNC Dream chaser whose mold lines are based on the NASA HL-20,[21] this task is significantly more difficult shows the top and side views of the HL-20 configuration. Note that the nose tip windward surfaces are asymmetric in both the vertical (Z-axis) and lateral (Y-axis) directions. For other surface installations such as wing or empennage, the geometry is even more complex (Figure 3).

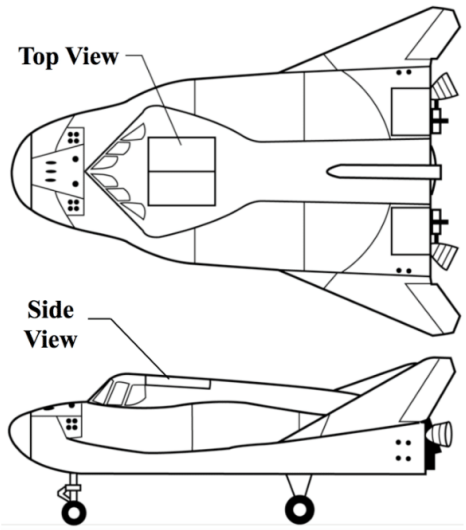

Figure 3 HL-20 mold lines.

(Image taken from https://academic-https://www.dfrc.nasa.gov/Gallery/Graphics/HL-20/index.html, reprinted with permission.)

Additionally, for real vehicles, ports cannot be installed at all locations on the vehicle surface, and often ports must be placed in positions that differ from the desired clean-sheet installation locations. The "as-installed" incidence angles can vary considerably from the angles as shown by the initial Computer Assisted Drawing (CAD) images.

Thus, a method for measuring the actual surface port incidence angles is highly desirable. The next section develops a method that deploys an inexpensive commercial optical-scanning system[22] to measure the surface ports surface incidence angles. As will be described in more detail, the candidate FADS configurations are scanned along the longitudinal axis and the resulting point-cloud edited using the open-source CloudCompare® software[23] to generate concentric "loops" surrounding each surface port. Each ring is assumed to be co-planar with the surface port, and the singular-value decomposition (SVD) is used calculate the local surface gradient vector. From the resulting gradient vector, geometric relationships calculate the port's polar coordinates including the surface incidence angle.

Optical-scan theoretical considerations

For this analysis, each annular loop "point cloud" with m elements is assumed to be co-planar with the interior FADS pressure port. Figure 4 shows a schematic of this arrangement where the point cloud encircles the FADS port with the center point located at position (xp, yp, zp) and the annular loop encircling the port at a mean radius Rscan. Since the point cloud is co-planar with the center point and the FADS port, there exists a 3-Dimensional plane through the locus of all the cloud's m data points with the formula,

$$a.x_i + b.y_i + c.z_i + d = 0$$
$$for...i = 1,2,...m \quad (5)$$

Writing Eq. (6) in matrix form,

$$\begin{pmatrix} x_1 & y_1 & z_1 & 1 \\ x_2 & y_2 & z_2 & 1 \\ . & . & . & . \\ . & . & . & . \\ x_m & y_m & z_m & 1 \end{pmatrix} . \begin{pmatrix} a \\ b \\ c \\ d \end{pmatrix} = 0 , \tag{6}$$

or in terms of matrix symbols,

$$M.\tilde{A} = 0 \tag{7}$$

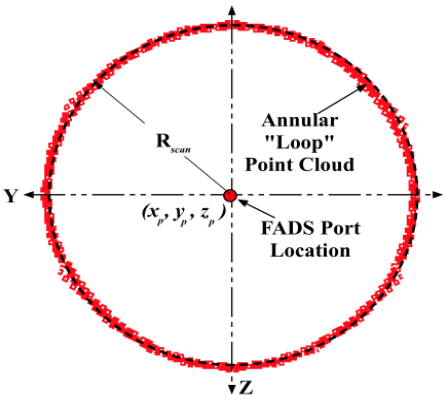

Figure 4 FADS port with the center point.

The coefficients of the 3-D plane are found as the null-space of the matrix on the left-hand side of Eq. (6). The null space is calculated by calculating the singular value decomposition[24] of M,

$$SVD[M] = U\,S\,V \tag{8}$$

In Eq. (8) the matrices orthogonal U, V are known as the left- and right-singular matrices, and the diagonal elements of S are the singular values of the matrix M. The number of non-zero singular values is equal to the ranks of M; and for this case of A 3-dimensional plane, the rank of M is 3. The column of the right-singular matrix corresponding the zero-magnitude singular value is the null space of Eq. (6), i.e. the coefficients {a, b, c, d}. The gradient vector for the planar equation is given by

$$\vec{N} = \begin{bmatrix} \frac{\partial}{dx}(a.x + b.y + c.z + d) \\ \frac{\partial}{dy}(a.x + b.y + c.z + d) \\ \frac{\partial}{dz}(a.x + b.y + c.z + d) \end{bmatrix} \begin{bmatrix} \vec{i} \\ \vec{j} \\ \vec{k} \end{bmatrix} = a\vec{i} + b\vec{j} + c\vec{k} \tag{9}$$

For convenience the gradient vector of Eq. (9) is normalized to give unity magnitude,

$$\vec{n} = \frac{a}{\sqrt{a^2+b^2+c^2}}\vec{i} + \frac{b}{\sqrt{a^2+b^2+c^2}}\vec{j} + \frac{c}{\sqrt{a^2+b^2+c^2}}\vec{k} \tag{10}$$

From the analytic geometry of Figure 2, the gradient vector can be written in terms of the port coordinates and the intercept with the longitudinal axis,

$$\vec{n} = \begin{bmatrix} n_x \\ n_y \\ n_z \end{bmatrix} = \begin{bmatrix} \frac{(x_p - x_{R_c})}{\sqrt{(x_p - x_{R_c})^2 + (y_p - y_{R_c})^2 + (z_p - z_{R_c})^2}} \\ \frac{(y_p - y_{R_c})}{\sqrt{(x_p - x_{R_c})^2 + (y_p - y_{R_c})^2 + (z_p - z_{R_c})^2}} \\ \frac{(z_p - z_{R_c})}{\sqrt{(x_p - x_{R_c})^2 + (y_p - y_{R_c})^2 + (z_p - z_{R_c})^2}} \end{bmatrix} \tag{11}$$

and

$$\begin{bmatrix} \frac{n_x}{n_y} \\ \frac{n_z}{n_y} \\ \frac{n_x}{n_z} \end{bmatrix} = \begin{bmatrix} \frac{x_p - x_{R_c}}{y_p - y_{R_c}} \\ \frac{z_p - z_{R_c}}{y_p - y_{R_c}} \\ \frac{x_p - x_{R_c}}{z_p - z_{R_c}} \end{bmatrix}, \begin{bmatrix} x_{R_c} - \frac{n_x}{n_y}.y_{R_c} = x_p - \frac{n_x}{n_y}.y_p \\ y_{R_c} - \frac{n_y}{n_z}.z_{R_c} = y_p - \frac{n_y}{n_z}.z_p \\ x_0 - \frac{n_z}{n_x}.x_{R_c} = z_p - x_p.\frac{n_z}{n_x} \end{bmatrix} \tag{12}$$

Eq. (12) simplifies to a 3-D deterministic linear system

$$\begin{pmatrix} 1 & -\frac{n_x}{n_y} & 0 \\ 0 & 1 & -\frac{n_y}{n_z} \\ -\frac{n_z}{n_x} & 0 & 1 \end{pmatrix} . \begin{bmatrix} x_{R_c} \\ y_{R_c} \\ z_{R_c} \end{bmatrix} = \begin{pmatrix} 1 & -\frac{n_x}{n_y} & 0 \\ 0 & 1 & -\frac{n_y}{n_z} \\ -\frac{n_z}{n_x} & 0 & 1 \end{pmatrix} . \begin{bmatrix} x_p \\ y_p \\ z_p \end{bmatrix} \tag{13}$$

that allows solution for the point of origin of the radius-of-curvature vector, $\{xR_c, yR_c, zR_c\}$. Again referring to the geometry of Figure 2,

$$\begin{bmatrix} x_p \\ y_p \\ z_p \end{bmatrix} - \begin{bmatrix} x_{R_c} \\ y_{R_c} \\ z_{R_c} \end{bmatrix} = R_c . \begin{bmatrix} \cos\Theta_p \\ \sin\Theta_p \sin\phi_p \\ \sin\Theta_p \cos\phi_p \end{bmatrix} \tag{14}$$

where,

$R_c = surface\,radius\,of\,curvature$

$\Theta_p = cone\,angle$

$\phi_p = clock\,angle$

And the solutions for the polar coordinates Rc, Θ , θ , in terms of the Cartesian points are given by Eq. (4).

Instrumentation and test systems

This section describes the instrumentation and test systems used to support the optical-scan feasibility and accuracy assessment tests. Here, two legacy 3-D printed shapes previously tested during a series of very low-speed wind tunnel tests were used to develop and evaluate this method. The shapes 1) a hemispherical head cylindrical forebody, and 2) a Rankine-Body. These probes were scanned along the longitudinal axis and the resulting point-cloud was edited using open-source software to generate three concentric "loops" surrounding each surface port. Each annular loop is assumed to be co-planar with the surface port, and the singular-value decomposition. This section first described the probe configurations, and then the details of the optical-scanning system are presented.

Legacy airdata probes

For the feasibility assessment, two similarly-sized probes, one with a hemispherical-cylinder shape, and one with a Rankin body shape were used. As reported by Whitmore and Case,[20] these legacy probes were previously used for a series of very low-speed wind tunnel tests that evaluated the feasibility of using a FADS-type configuration for UAS airdata measurements. These probes had ports 5-ports at cone angles arranged only in the vertical meridian, thus, only the angle of attack, dynamic pressure, and the associated airspeeds could be sensed by these probes. This design was for operational simplicity. It was reasoned that if angle-of-attack can be reasonably and accurately sensed at low speeds, then sensing angle-of-sideslip would present the same issues and accuracy results. Figure 5 compares the probe geometries lists the port cone and clock angles for these probes.

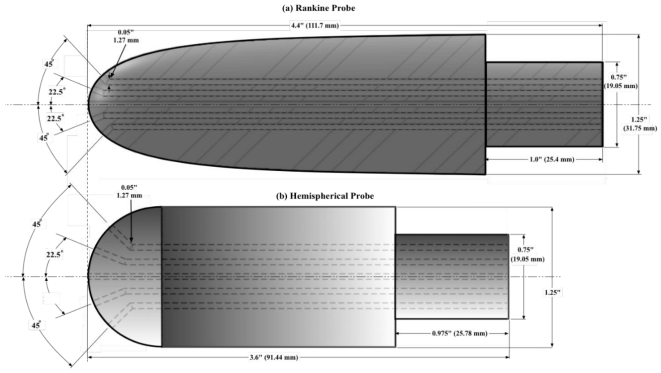

Figure 5 Hemispherical-head and Rankine-body shape comparisons with 5 ports arranged at identical incidence angles.

The test probes were additively manufactured from polycarbonate (Veroclear®) using a Polyjet (Objet 260 Connex3) 3D-printer. For both designs the probes were printed with "built-in" surface ports pressure transmission paths. Figure 13 shows these design layouts for the Rankine and hemispherical-head probes. Each probe had a major diameter of 1.25" (31.75 mm), and the 5 pressure-transmission paths used 0.5" (1.27 mm) surface ports, laid out at 22.5o degree surface-normal spacing intervals. Barbed plastic tube fittings were bonded into probe outlet holes, and flexible tubing was used to transmit pressure to the sensing pressure transducer. The probe support sting and fairing were printed from Acrylonitrile Butadiene Styrene (ABS) at full density using a Fortus 250-MC, Fused-Deposition Manufacturing (FDM) printer. The sting was mounted using a telescope sight and support rail. This sting arrangement was used to support the probe during the optical-scan tests to reported. Figure 6 shows the Hemispherical-Probe as mounted in the wind tunnel during the previously reported tests.[20]

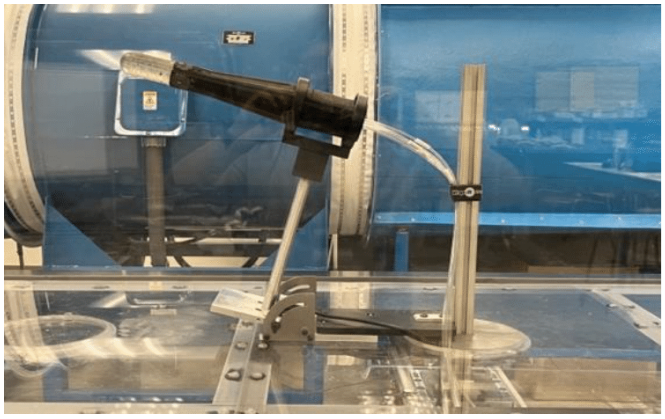

Figure 6 3-D Printed hemispherical-probes as mounted in wind tunnel test section for low speed tests reported.[20]

(Image taken from,[20] reprinted with permission)

As reported by[20] the two probe configurations have distinctly different surface pressure distributions; however, both probes were equally-effective and equally-accurate as FADS airdata sensors. Figure 7 shows a typical pressure distribution data plot, collected at 5 m/s and 25 m/s airspeed and 0° and 5° angle-of-attack set points. These pressure coefficient Cp data, plotted as a function of the port incidence angle θ, are compared against the theoretical models for each probe.

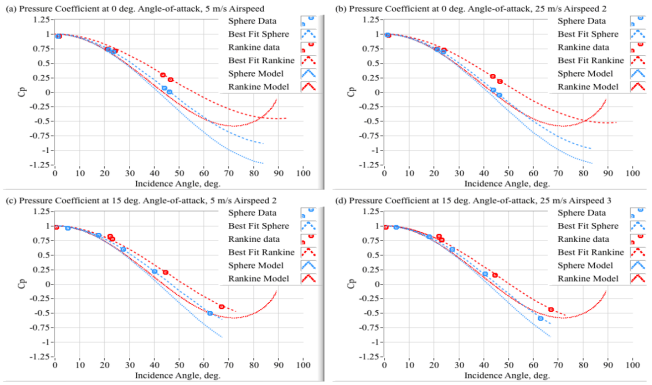

Figure 7 Comparing the pressure distributions for Rankine-body and hemispherical-head probes, {0°, 15°} angles-of-attack, and {5, 25 m/s} airspeeds.

(Image taken from Ref.[20], Reprinted with permission.)

Optical-scan system

The 3-D scans for this demonstration were collected using an inexpensive, portable, home-use system developed by Creality Inc.[22–25] The CR-Scan Ferret system is primarily designed for 3-D printing applications and features desktop software that allows the user to select larger-scale, low resolution, or smaller-scale, high-resolution scan images. The CR-Scan Ferret Pro works on the principle of infrared binocular stereo technology[26] that uses infrared light to capture images through two separate lenses. This stereo-image gives accurate depth perception and allows creation of 3-D surface-maps.

Figure 8 shows the scan hardware arrangement for the 3-D optical-scans of the airdata probes. A laptop computer used to collect the scan buffers via the Universal serial Bus (USB). As described previously, the wind-tunnel support sting was used to support the probe during the optical-scans. The probe sting mount supporting rod was adjusted to precisely level the probe tip, with the longitudinal axis directly aligned with the scanner camera lens. The distance from the lens to the probe tip was approximately 150 mm (6").

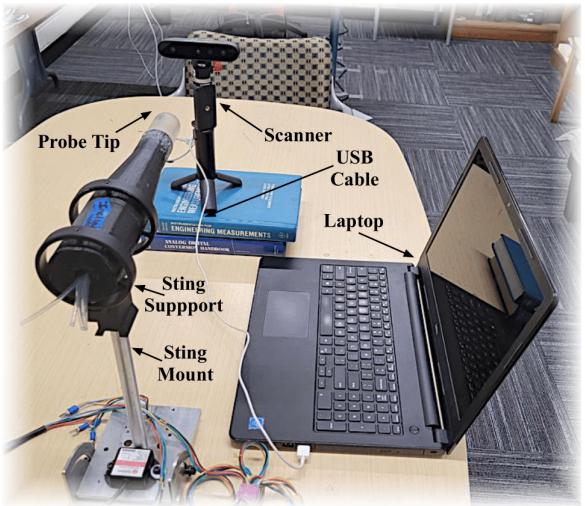

Figure 8 Hardware arrangements for the 3D optical-scans of the airdata probes.

Processing software

The open-source software[23] used to process each optical-scan was developed by CloudCompare, and features an graphical user interface

that allows specific data points to be selected from the total point cloud file. Scans were performed only using black and white capture mode. As an example, Figure 9 shows the initial point cloud scan of the hemispherical-probe prior to editing. As described previously, for this analysis the raw point cloud was thinned to generate three concentric "loops" surrounding each surface port. Although the thinning process was ad-hoc and a bit tedious, producing multiple "unsatisfactory" data sets; eventually, a full, satisfactory data set was generated for both probes in less than 8 hours of total work.

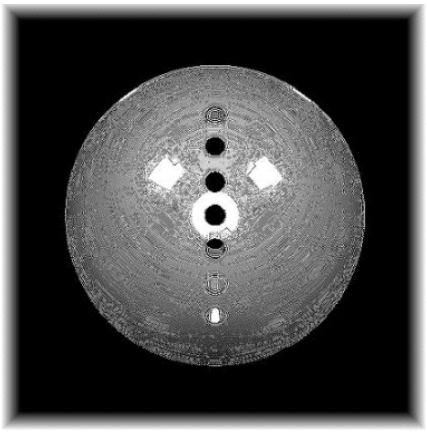

Figure 9 Raw scanned hemispherical-probe image before processing, frontal view.

Results and discussion

This section presents the optical-scan results. First a detailed description of a single-port data set, including the post-thin scan "anatomy' and a detailed break-down to the SVD decomposition are presented. Next the resulting optical-scan data for both ports are presented. Assuming the 3-D printed port geometries as the "truth set," these data summaries show the obtained accuracies results for each probe, each port, for each of the 3 individual scan loops, and for all 3-loops used as concatenated data sets. Finally, using the scan-derived port geometries, the FADS pressure data[20] are reprocessed to investigate the effects of the "as-installed" port locations on the overall system accuracies.

Detailed FADS-port optical-scan analysis

Figure 10 shows the detailed anatomy of an optical-scan as collected for the Rankine probe center port. Here the total point cloud was thinned into three concentric rings with rough radii of approximately 1, 2, and 4 mm. Figure 10(a) shows the front view and Figure 10(b) shows the port-side view. Note from Figure 10(a) that the edited scans are rather crude, only approximating trice circles. Also note from Figure 10(b) the individual scan-loops are not ideally co-planar. Thus, there exists the potential for the previously-described SVD decomposition to fail or at least achieve inaccurate results. The detailed numerical discussion to be presented demonstrates the robustness of this method, and will show that accurate results are achieved.

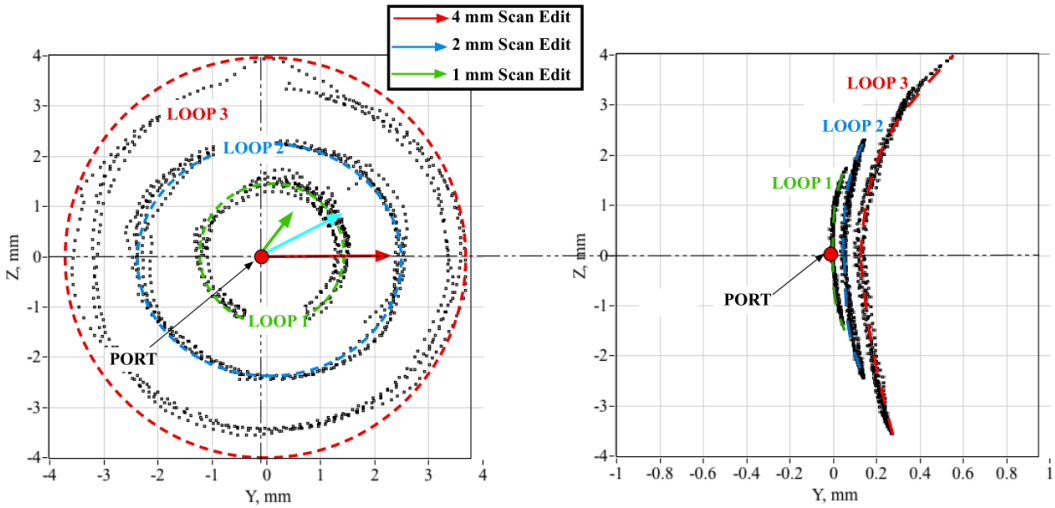

Figure 10 Anatomy of thinned optical port scan.

The SVD decomposition was performed using a custom-coding of the classical Golub-Reinsch (GR-SVD)[27] algorithm. Here the SVD Matrix (M) of Eqs. (5) and (6) is decomposed as shown by Eq. (7). For this example the 3-loop scan of Figure 10 contains a total of 1318 (m) data points, and the matrix M has dimension 1318 by 4. The corresponding dimension of U is 1318 by 1318, the dimension of S is 1318 by 4, and the dimension of V is 4 by 4. Table 1 shows the numerical elements for M, U, S, and V. Only the leading elements of each matrix are shown. On Table 1 the ellipsis (...) in rows or columns represents the numerical values that are not displayed.

Note that the Singular-Value Matrix (S) had no diagonal element in rows 1-4 with an exactly zero magnitude. Thus, the singular value of the least magnitude is selected. Thus, 4th diagonal element which has value S (4,4) = 0.03080 approximates the null-singular value. This singular is more than an order of magnitude smaller than the other three singular values of S. The corresponding Left Singular Vector (the 4th column of V) approximates the null-space of the matrix M. Thus, allowing that the gradient vector at the center (approximately the FADS center point location) is given by Eq. (8),

$$Null(M) \simeq \begin{bmatrix} -0.9981 \\ 0.00047 \\ 0.00150 \\ 0.06144 \end{bmatrix}, \vec{N} = \begin{bmatrix} -0.9981 \\ 0.00047 \\ 0.00150 \end{bmatrix}, \vec{n} = \begin{bmatrix} -0.99999 \\ 0.000473 \\ 0.001502 \end{bmatrix} \quad (15)$$

Citation: Whitmore SA. An optical-scan method for measuring the as-installed surface port incidence angles for flush air data sensing (FADS) systems. *Aeron Aero Open Access J.* 2024;8(1):42–52. DOI: 10.15406/aaoaj.2024.08.00192

In Eq. (15) Null (M) is the null-space of M, and $\bar{n}$ approximates the normalized surface gradient vector at the cloud-point locus center (~FADS center port). Using this normalized gradient vector the corresponding longitudinal axis intercept and clock/cone angles are calculated using Eqs. (13) - (14). Because the SVD is a generalization of the classical QR factorization used for full-rank matrices and the least-squares problem,[24] this decomposition provides a measure of noise rejection, and is quite robust with regard to the surface gradient parameter estimation.

Table 1 Numerical elements of optical-scan SVD decomposition

(a) SVD (M) Matrix			
0.0197	0.31633	-0.64908	1
0.0181	0.37719	-0.60898	1
0.0178	0.29569	-0.60511	1
0.0173	0.23153	-0.63096	1
0.0192	0.16034	-0.65177	1
0.0194	0.09217	-0.66047	1
0.0224	0.04232	-0.7068	1
...	...	...	...

(b) Left singular vectors (U)					
0.0221	-0.0244	0.0058	0.0213	-0.0076	...
0.0233	-0.023	0.005	0.0222	-0.0048	...
0.0218	-0.0233	0.0067	0.0223	-0.019	...
0.0206	-0.0243	0.0077	0.0225	-0.0333	...
0.0192	-0.0252	0.009	0.0215	0.9985	...
0.0179	-0.0258	0.0102	0.0214	-0.0015	...
0.0169	-0.0272	0.0108	0.0198	-0.0014	...
...	...	...	...	...	...

(c) Singular value (S) Matrix			
0.6194	0	0	0
0	0.57016	0	0
0	0	0.53884	0
0	0	0	0.0308
0	0	0	0
0	0	0	0
0	0	0	0
...	...	...	...

(d) Right singular vectors (U)			
0.0434	-0.0182	0.03956	-0.9981
0.7086	0.179	-0.6825	0.00047
0.1039	0.93026	0.35186	0.00149
0.6965	-0.3197	0.63938	0.06144
...	...	...	...
...	...	...	...
...	...	...	...
...	...	...	...

Summary of optical-scan results

This section summarizes the "best-achieved" scan data for both the Rankine-Body and Hemispherical Probe. Figure 11 plots the Z/X (port side view) and Z/Y (front view) scan data for the Rankine-Body and Figure 12 plots the corresponding point-cloud data for the Hemispherical-Probe. The processes used to create the data sets were identical for both the Rankine-body and Hemispherical-probe. For each body, 4 discrete scan-images, similar to Figure 9, were recorded and subsequently averaged to give a measure of noise rejection. For each probe the averaged data-clouds were cloned into 15 discrete, but-identical files. Each of the 15 files were subsequently processed using the CloudCompare software.[23] The first-pass of the thinning procedure simply rejected all data points that lie outside of the selected 3-dimensional radial distance (1-mm, 2-mm, and 4-mm) from each the 5 FADS port center-locations. The second pass of the thinning procedure performs a circumferential scan around each port location, and retains only the data-pixels that give the maximum distance from the port center at each circumferential position. The results are the 30 (2 by 15) distinct annular-ring data sets are shown by Figure 11 (a), (b), (c), and Figure 12 (a), (b), and (c). Figure 11 (d), and Figure 12 (d), show the merged results, as concatenated from (a), (b), and (c) for each probe.

Table 2 compares the Cone and Clock Angle Estimates against the 3-D printed reference values for the Rankine-Body, and Table 3 presents the same comparisons for the Hemispherical-Probe. From Eq. (2), because the clock angle makes no contribution to the total incidence angle at zero angle-of-attack and sideslip, for this analysis the root-mean-square error of the incidence angle error is identical to the absolute value of the cone-angle error. Assuming the "known" 3-D printed cone-angles as the "truth" set, Figure 13 plots the corresponding port-angle errors as derived from the optical-scans. Figure 13 plots the estimation errors resulting for each of the three individual-loops (1 mm, 2 mm, and 3mm), and also for the set of the three concatenated loops.

Discussion of optical-scan results

Considering the small size of the legacy probes used for this study, the resulting incidence angle estimates as presented in this report are remarkably accurate. From the images of Figure 11 and Figure 12 it is obvious that the current scanning process is a bit "rough," and the scanned loops are far from perfect annuli. Also, as noted earlier and shown by Figure 10; due of the curved probe shapes the scanned-loop point clouds are not ideally co-planar. Thus, even though the SVD decomposition does not produce a true null-space vector, the presented-method of choosing the smallest-magnitude singular value and its corresponding right-singular vector appears to be "sufficiently accurate." This result illustrates the robustness of the presented scan procedure.

Interestingly, even though the smaller loops are more co-planar, the associated systematic-error is corresponding larger. Thus, the estimation accuracy tends to favor the larger scan loops as opposed to the smaller ones. The trade-off here appears to be the "flatness" of the loop versus the scan resolution. During the two-pass thinning process, it was much easier to "draw" accurate scan loops at larger radii, resulting in more symmetrical and favorable data scans. Also, as the edited-loops grow in size, the number of points in each scan grows approximately by the square of the radii. Thus the 4mm loop cloud contains approximately 16 times as many points as the 1-mm loop. The larger number of ports allows for greater noise rejection. As expected, due to the largest number of data points, best accuracies are

achieved from the 3-loop concatenated data sets. Also of interest is the lower estimation error for the spherical probe. The observed lower estimation error for the Hemispherical-Probe, likely results from the less-oblique surface geometry that was significantly easier to scan and edit when compared to the Rankine-body data sets. The spherical scans are also significantly more co-planar. Thus, it appears that the non-co-planar shape does have at least a minor contributing factor for the estimation error.

Finally, using the "best estimate" of the installed port polar coordinates using the three concatenated point cloud loops, from Table 2 and Table 3, column 7, the FADS error analysis[20] was repeated. Figure 14 and Figure 15 compare the results. Using the design polar coordinates from (Figure 5) for the FADS calculations, for both probes the FADS airspeed estimate is accurate to better than 0.75 m/sec over the entire airspeed range. The angle-of-attack errors are less than 1 degree, and it is reasonable to assume that this value is within the uncertainty to which the probe is aligned geometrically within the tunnel. When the "as printed" polar coordinates replace the design polar coordinates, the resulting differences are very minor, with the revised analysis showing slightly-reduced overall error levels.

Table 2 Optical-scan cone, clock angle estimates for Rankine-body

Port Number	Coordinate (deg.)	Reference (3-D Print)	Loop 1	Loop 2	Loop 3	Concatenated Loops
1	Cone Ang.	45°	45.55°	45.33°	44.78°	44.81°
	Clock Ang.	0°	-0.83	-0.83	-0.74	-0.69
2	Cone Ang.	22.5°	22.05°	22.17°	22.64°	22.65°
	Clock Ang.	0°	-2.02	-1.2	-1.1	-1.82
3	Cone Ang.	0°	0.39°	0.39°	0.12°	0.09°
	Clock Ang.	0°	0.01°	0.02°	0.02°	0.12°
4	Cone Ang.	22.5	22.09	22.75	22.65	22.66
	Clock Ang.	180°	179.19°	179.19°	179.78°	178.77°
5	Cone Ang.	45°	45.59°	45.37°	44.80°	45.19°
	Clock Ang.	180°	178.83°	178.89°	179.58°	179.32°

Table 3 Optical-scan cone, clock angle estimates for hemispherical-probe

Port Number	Coordinate (deg.)	Reference (3-D Print)	Loop 1	Loop 2	Loop 3	Concatenated Loops
1	Cone Ang.	45°	45.48°	44.68°	44.78°	44.83°
	Clock Ang.	0°	-0.83	-0.84	-0.74	-0.68
2	Cone Ang.	22.5°	22.89°	22.80°	22.65°	22.64°
	Clock Ang.	0°	-1.95	-1.17	-1.12	-1.83
3	Cone Ang.	0°	0.35°	0.25°	0.12°	0.09°
	Clock Ang.	0°	0.06°	0.08°	0.03°	0.18°
4	Cone Ang.	22.5	22.11	22.78	22.67	22.37
	Clock Ang.	180°	179.19°	179.80°	179.76°	178.71°
5	Cone Ang.	45°	45.50°	45.33°	44.84°	45.16°
	Clock Ang.	180°	178.83°	178.89°	179.58°	179.33°

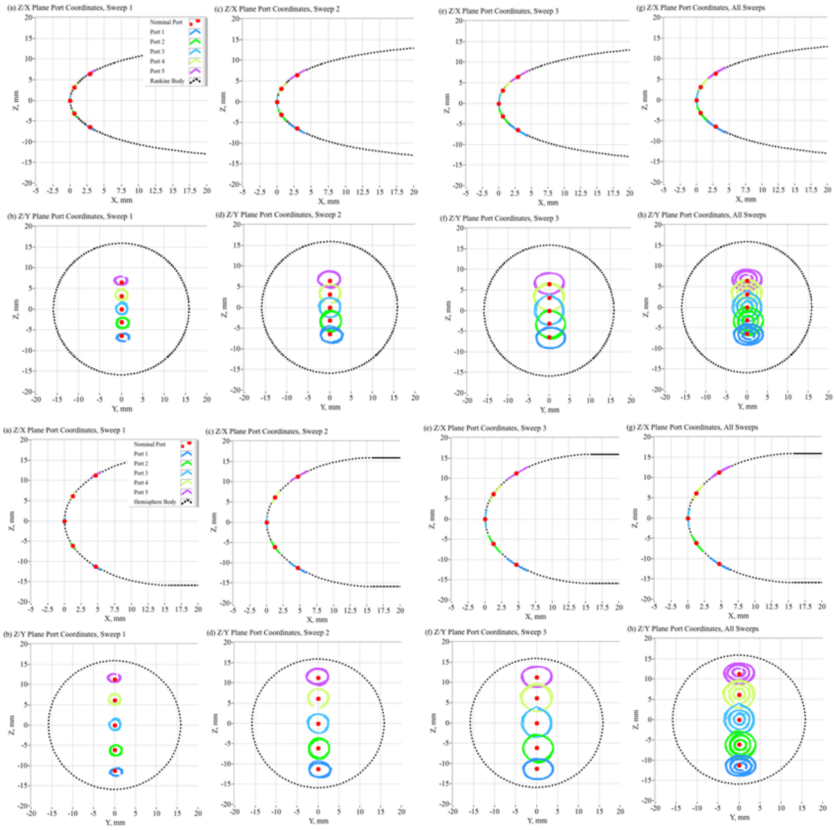

Figure 11 Optical-scan point-cloud summaries for Rankine-body FADS ports.

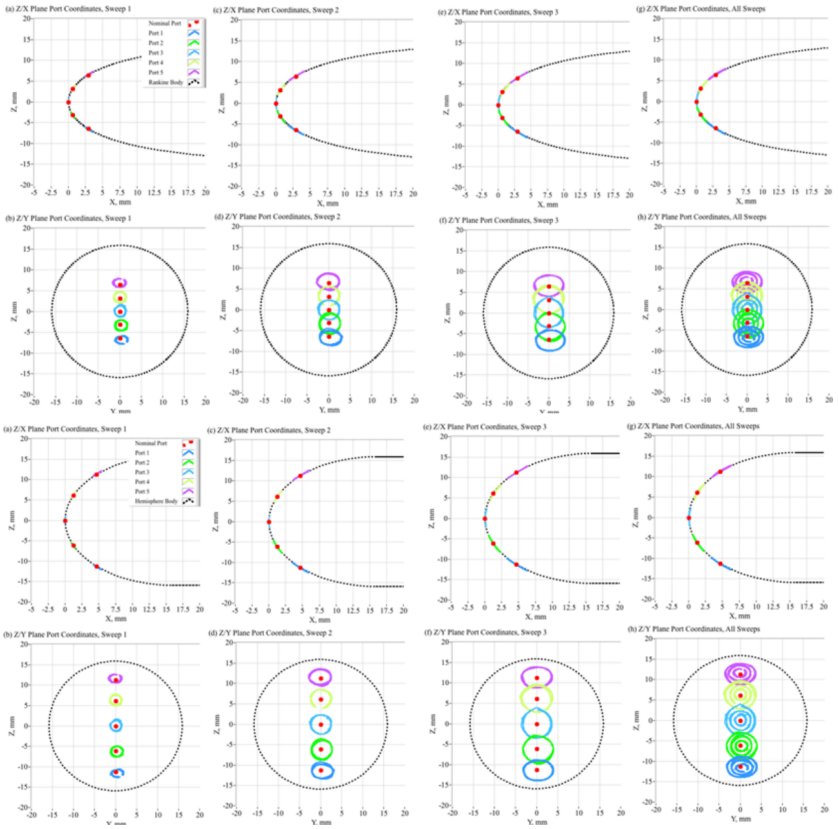

Figure 12 Optical-scan point-cloud summaries for hemispherical-probe FADS ports.

Citation: Whitmore SA. An optical-scan method for measuring the as-installed surface port incidence angles for flush air data sensing (FADS) systems. *Aeron Aero Open Access J.* 2024;8(1):42–52. DOI: 10.15406/aaoaj.2024.08.00192

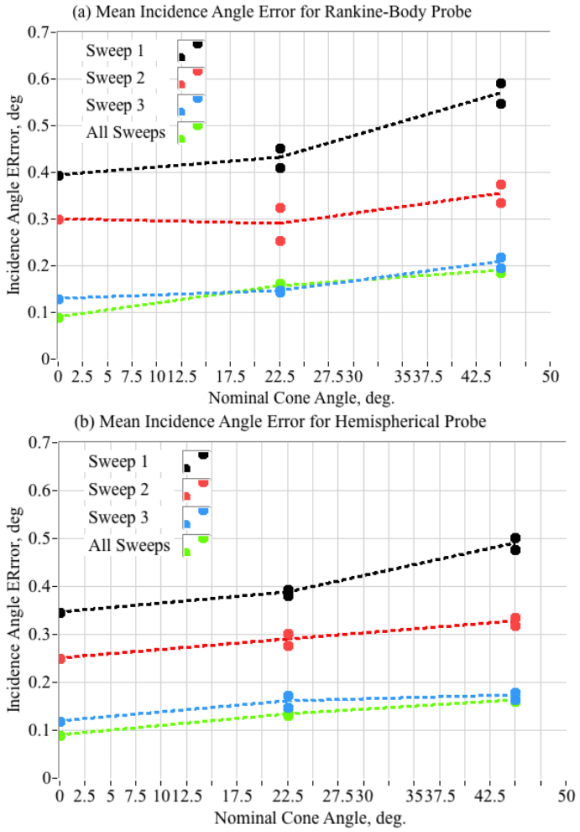

Figure 13 Optical-scan incidence angle absolute estimation errors for Rankine-body and hemispherical probe.

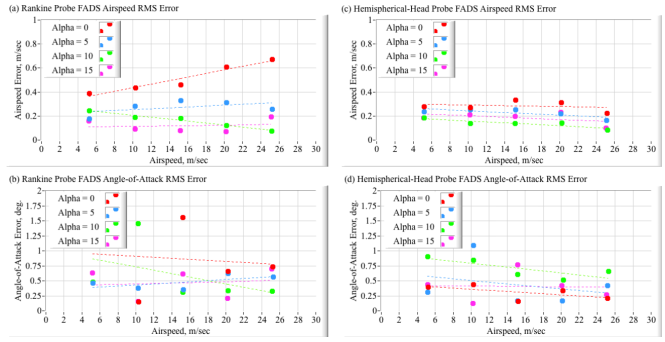

Figure 14 Original FADS estimation error summary for Rankine and hemispherical-head probe analyses.[20]

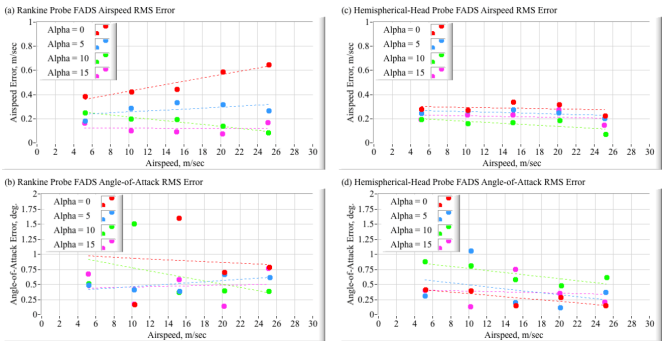

Figure 15 Revised original fads estimation error summary for Rankine and hemispherical-head probe analyses, using best estimate of as-installed port coordinates.

Conclusion

The flush airdata sensing (FADS) system concept, where airdata are inferred from nonintrusive surface pressure measurements, has emerged as a favored technique for very low-seed vehicles like Unmanned Aerial Systems (UAS). Also, from previous experience, this FADS method is confirmed as essential for hypersonic applications. FADS does not require probing of the flow-field, but instead uses the natural contours of the vehicle for the sensing matrix. Although multiple methods have been developed to derive airdata from the sensed pressure matrix, all methods rely on accurate knowledge of the surface-port incidence angles, the angles between the surface normal and the longitudinal axis of the vehicle.

For simple spherical nose cap configurations, determining the surface incidence angle was rather simple. However, for significantly more complex shapes, this task is significantly more difficult. For other surface installations such as wing or empennage, the geometry is even more complex. Additionally, for real vehicles, ports cannot be installed at all locations on the vehicle surface, and often ports must be placed in positions that differ from the desired clean-sheet installation locations. The in-situ incidence angles can vary considerably from the angles as shown by the initial Computer Assisted Drawing images. Thus, a method for measuring the actual surface port incidence angles is highly desirable.

This study investigates the feasibility and accuracy of using an inexpensive optical-scanning system to measure the "as-installed" FADS pressure ports surface incidence angles. Here, two legacy 3-D printed shapes 1) a hemispherical-head cylindrical forebody, and 2) a Rankine-Body, as previously tested during a series of very low-speed wind tunnel tests were used to develop and evaluate this method. The shapes were scanned along the longitudinal axis and the resulting point-cloud was edited using open-source software to generate three concentric "loops" surrounding each surface port. As presented, the ad-hoc, manual process for thinning the full scanned point cloud to produce the concentric loops for each FADS port was a bit tedious, and produced multiple "unsatisfactory" data sets before eventually, a full, satisfactory data set was generated. However, using modern artificial intelligence or machine learning techniques, it is likely that this process can be easily automated.

Once the full point-clouded was edited, each annular loop was assumed to be co-planar with the surface port, and the singular-value decomposition (SVD) used calculate the local surface gradient vector. From the resulting gradient vector, geometric relationships calculate the port's polar coordinates including the surface incidence angle and circumferential cone-angle. Considering the small size of the legacy probes used for this study, the resulting incidence angle estimates as presented in this report are remarkably accurate. Even though the scanned loops were not perfect annuli and not ideally co-planar, with the associated that the SVD decomposition not-producing a theoretically-true null-space; the technique of choosing the smallest-magnitude singular value and its corresponding right-singular vector still appears to be quite accurate. Using the concatenated 3-annuli data sets, the incidence angle estimates were accurate to better than 0.25 degrees for all ports on both probe. This result illustrates the robustness of the presented scan procedure. Going-forward, the presented technique offers a powerful tool for practically implementing increased-accuracy FADS systems on a wide variety vehicle shapes and configurations.

Acknowledgments

None.

Conflicts of interest

The authors declare that there is no conflict of interest.

References

1. Siemers PJ, Wolf H, Flanagan P. Shuttle entry air data system concepts applied to Space Shuttle Orbiter flight pressure data to determine air data - STS 1-4. NV, USA: 21st Aerospace Sciences Meeting. 1983. 118 p.
2. Larson TJ, Siemers PJ. Subsonic tests of an all-flush-pressure-orifice air data system. *NASA TP 1871*. 1981.
3. Henry MW, Wolf H, Siemers Paul MIII. An evaluation of shuttle entry air data system (SEADS) flight pressures - comparisons with wind tunnel and theoretical predictions. San Diego, CA: 15th AIAA Aerodynamic Testing Conference. 1988. p. 88–2052.
4. Larson TJ, Whitmore SA, Ehernberger LJ, et al. Qualitative evaluation of a flush air data system at transonic speeds and high angles of attack. *NASA TP 2716*. 1987.
5. Whitmore SA, Moes T, Larson TJ. Preliminary Results from a subsonic high angle-of-attack flush air data sensing (HI-FADS) system: design, calibration, and flight test evaluation. Reno, NV: 25th AIAA Aerospace Sciences Conference; *NASA TM-101716*. 1990.
6. Whitmore SA, Moes TR. the effects of pressure sensor acoustics on airdata derived from a high-angle-of-attack flush airdata sensing (HI_FADS) system. Reno, NV: 26th AIAA Aerospace Sciences Conference; *NASA TM-101736*. 1991.
7. Whitmore SA, Moes TR, Czerniejewski MW, et al. Application of a flush airdata sensing system to a wing leading edge (LE_FADS). Reno, NV: 28th AIAA Aerospace Sciences Conference; *NASA TM 104267*. 1993.
8. Cobleigh BR, Whitmore SA, Haering EA, et al. Flush airdata sensing (FADS) system calibration procedures and results for blunt forebodies. Norfolk, VA, United States: International Space Planes and Hypersonic Systems and Technologies; *NASA TP-209012*. 1999.
9. Whitmore SA, Cobleigh BR, Haering EA. Design and calibration of the X-33 flush airdata sensing (FADS) System. Reno, NV: Research Engineering, NASA Dryden Flight Research Center, 30th AIAA Aerospace Sciences Conference; *NASA TM-1998-206540*. 1998.
10. Gelzer C. NASA Armstrong fact sheet: X-38 prototype crew return vehicle. *NASA*. 2014.
11. Davis MC, Pahle JW, White JT, et al. Development of a flush airdata sensing system on a sharp-nosed vehicle for flight at mach 3 to 8. *NASA TM-209017*. 2000.
12. Gebhart C. Dream chaser through critical landing test, prepares for orbital flights. 2017.
13. Whitmore SA, Davis RJ, Fife JM. In-flight demonstration of a real-time flush airdata sensing (RT_FADS) system. Reno, NV: 30th AIAA Aerospace Sciences Conference; *NASA TM 104314*. 1995.
14. Crowther WJ, Lamount PJ, Laurence DRP. Neural network approach to the calibration of a flush air data system. *Aeronautical Journal*. 2001;105(1044):85–95.
15. Rohloff TJ, Whitmore SA, Catton I. Air data sensing from surface pressure measurements using a neural network method. *AIAA Journal*. 1998;36(11):2094–2101.
16. Rohloff TJ, Whitmore SA, Catton I. Fault-tolerant neural network algorithm for flush air data sensing. *J Aircraft*. 1999;36(3):541–549.
17. Laurence RL, Argrow BM. Development and flight test results of a small UAS distributed flush airdata system. *J of Atmos and Ocean Tech*. 2018;33(5):1127–1140.
18. Anderson JD. Modern compressible flow. 4th Ed, New York: The McGraw Hill Companies, Inc; 2021.
19. Whitmore SA, Timothy RM. Failure detection and fault management techniques for a pneumatic high-angle-of-attack flush airdata sensing (HI-FADS) system. *NASA TM-4335*. 1992.
20. Whitmore SA, Case ZQC. Comparing a 3-d printed hemispherical-head and Rankine-body probe shapes for very low speed flush air data system (FADS) measurements. *AAOAJ*. 2023;7(2):71–85.
21. De Chiara G. From HL-20 to dream chaser, the long story of a little space plane. *NASA Space Flight*. 2012.
22. CREALITY CR-Scan Ferret 3D Scanner User Manual.
23. CloudCompare Wiki.
24. Golub GH, Van Loan CsF. Matrix computations. 3rd ed. Johns Hopkins Press; 1996.
25. Creality CR-Scan Ferret Pro.
26. Li H, Wang S, Bai Z, et al. Research on 3D reconstruction of binocular vision based on thermal infrared. *Sensors*. 2023;23(17):7372.
27. Chan TF. An improved algorithm for computing the singular value decomposition. *ACM Transactions on Mathematical Software*. 1982;8(1):72–83.